

## Impact of DC glow discharge plasma treated Ti doped hydroxyapatite nanomaterials using antibacterial and cytotoxicity applications

P. Sri Devi<sup>a,b,\*</sup>, K. A. Vijayalakshmi<sup>c</sup>

<sup>a</sup>Research Scholar, Centre for Research and Evaluation, Bharathiar University, Coimbatore, Tamilnadu 641046, India

<sup>b</sup>PG Department of Physics, Vellalar College for Women, Erode, Tamilnadu 638012, India

<sup>c</sup>Sri Vasavi College, Erode, Tamilnadu 638316, India

In this work we developed Ti doped hydroxyapatite with were synthesized by using a sol-gel technique with exposed to DC glow discharge plasma with different times treated. The pure and Ti/HAp were characterised by using different characterizations like XRD, FTIR, SEM, EDAX, UV-visible, PL, TG-DTA, antibacterial activity, 3T3 fibroblast cells and MCF-7 breast cancer cell line with cytotoxicity efficiency analysis. The pure HAp and Ti/HAp materials had a nanocube and nanoflakee shape in the SEM results. In the ultraviolet-visible light (UV-vis) spectrum, the band edge absorption of bare HAp and Ti/HAp samples is discovered at wavelengths of 295 nm and 328 nm, respectively. The antibacterial activity of untreated and plasma-treated pure HAp and Ti/HAp samples are tested against two gram-positive bacteria, Bacillus cereus and Staphylococcus aureus, as well as two gram-negative bacteria, E. coli and Pseudomonas aeruginosa, using the agar well diffusion technique. The MTT assay was used to investigate the mean per cent (% percent) cell survival of Ti/HAp at various concentrations (6 mg/mL; 85 mg/mL) against 3T3 fibroblast cells and human MCF-7 Breast cancer cell lines. The synthesised Ti/HAp biocompatibility makes it a viable contender for future biological uses.

(Received June 13, 2022; Accepted October 12, 2022)

**Keywords:** Ti doped hydroxyapatite, Plasma exposed HAp, Antibacterial activity, 3T3 fibroblast cells, MCF-7 breast cancer cell

### 1. Introduction

Bacterial resistance is a major public health concern that has yet to be addressed globally. This syndrome is caused by the indiscriminate and unreasonable use of antibacterial medicines [1, 2]. Because of the lack of efficacy of required antibiotics, the World Health Organization (WHO) has observed an increase in bacterial illnesses requiring sophisticated treatments. While bacterial resistance is a natural process, it is increased by ineffective antibacterial drug use, which leads to not only longer hospital stays, but also greater costs, treatment failures (e.g., hip prosthesis infection), and mortality [3]. As a result, antibiotics are taken before surgery-both orally and in implants-do not give adequate protection; additionally, the administration of the incorrect antibiotic or low doses of essential medicines might result in the development of resistant bacteria, complicating therapy [4-6]. As a response, numerous healthcare industries are working on alternatives to slow the spread of bacterial resistance (such as preventative programmes or novel antibacterial compounds) [7]. Pharmaceutical manipulation is more sensitive than manipulating synthetic materials doped with metal ions, which can only harm human cells in large numbers [8]. Bacterial resistance is a prevalent issue in the field of biomaterials, particularly for materials used as internal prostheses (e.g., hip prosthesis). The recipient's inability to cope with the infection process and biological incompatibility is the most common reasons for prosthesis failure [9, 10].

Hydroxyapatite (HAp,  $\text{Ca}_{10}(\text{PO}_4)_6(\text{OH})_2$ ) is a form of bio-ceramic that is chemically comparable to the mineralized phase of real bone and teeth. It belongs to the calcium

---

\* Corresponding author: karthisridevi@gmail.com  
<https://doi.org/10.15251/DJNB.2022.174.1223>

orthophosphate class. HAp has grown in popularity for dental and orthopaedic applications because of its unique biological features such as bioactivity, biocompatibility, non-toxicity, osteoconductivity, and ability to enable direct chemical bonding with genuine bone tissue [11-14]. HAp has been widely employed in dentistry as bone grafts or implant materials to restore bone defects caused by periodontitis, as scaffolds for periodontal regeneration, and as a covering material for dental implants [15-17]. Antibacterial characteristics are added to hydroxyapatite by its ability to hold multiple metal cations in its chemical structure at the calcium position. Metal oxides, such as copper oxide (CuO) [18], zinc oxide (ZnO) [19], and titanium oxide (TiO<sub>2</sub>) [20] are used in a wide range of materials. Due to its low cost, chemical stability, and nontoxicity to humans, TiO<sub>2</sub> nanoparticles are one of the most often employed materials for photocatalytic antibacterial applications [21]. For anatase, TiO<sub>2</sub> is a broad semiconductor with a bandgap of 3.26 eV [22]. In recently, Yanni Zhang et al developed a TiO<sub>2</sub> nanotube used to increase antibacterial activity and cytocompatibility [23]. Jing Han et al. created a Ti-doped hydroxyapatite material as a potential nanocomposite for joint wound healing [24].

In this work, we used the sol-gel approach to make pure HAp and Ti-doped HAp (Ti/HAp) nanocomposite and exposed them to low-temperature DC glow plasma for 5, 10, and 15 minutes with a discharge potential of roughly 400V. The identification of functional groups, crystalline of the surface, and thermal stability of the synthesised untreated and plasma-treated bare and Ti-doped HAp samples was analysed by sample were determined using Fourier Transform Infrared spectroscopy (FTIR), X-ray diffraction analysis, and thermogravimetric (TG/DTA) technique. UV-Visible spectroscopy and PL photoluminescence studies were also used to investigate the optical properties of the synthesised nanopowder. The surface morphology and elemental composition of the untreated and plasma-treated Ti-doped HAp were determined using scanning electron microscopy (SEM) and energy dispersive X-ray analysis (EDAX). Vickers Hardness Test is used to determine mechanical strength.

## **2. Experimental procedure**

### **2.1. Chemicals**

All chemicals employed in the synthesis technique were of standard purity and analytical grade. The bare HAp and Ti-doped HAp samples are made with the chemicals listed below. Calcium nitrate tetrahydrate Ca (NO<sub>3</sub>)<sub>2</sub>.4 H<sub>2</sub>O (95% EMPLURA), diammonium hydrogen phosphate (NH<sub>4</sub>)<sub>2</sub> HPO<sub>4</sub> (99% SIGMA ALDRICH), Titanium nitrate Ti(NO<sub>3</sub>)<sub>4</sub> (99% SIGMA ALDRICH).

### **2.2. Synthesis of Ti doped hydroxyapatite (HAp)**

The HAp nanomaterials are made utilising the easy sol-gel process. In 500 ml of D.I water, 1 mmol of Ca (NO<sub>3</sub>)<sub>2</sub>.4 H<sub>2</sub>O and 0.6 mmol of (NH<sub>4</sub>)<sub>2</sub>HPO<sub>4</sub> materials are dissolved. The ammonium hydroxide solution was then added to the above solution with the pH set to 10 and agitated continuously for one hour. The precipitate was then aged for 24 hours at room temperature before being washed four times with de-ionized water and dried for 10 hours in a hot air oven at 373 degrees Fahrenheit [25]. The dried powder was then crushed with a mortar and pestle before being calcined in a muffle furnace at 523 K for 2 hours using a silica crucible.

### **2.3. Synthesis of Ti doped hydroxyapatite (Ti/HAp)**

In the synthesis of Ti/HAp samples followed by two steps: (i) 1 mmol of Ca (NO<sub>3</sub>)<sub>2</sub>.4 H<sub>2</sub>O and 0.6 mmol of (NH<sub>4</sub>)<sub>2</sub>HPO<sub>4</sub> materials are dissolved in 50 ml of D.I water and continually stirred on 15 min. (ii) 0.1 M of Ti(NO<sub>3</sub>)<sub>4</sub> of was dissolved in the above phosphoric solution and stirred for 15 min. After the process, NH<sub>4</sub>OH solution was added drop by drop in above solution and pH set 10 and continually stirred in 1 hour. The precipitate was rinsed four times with de-ionized water and dried for ten hours in a hot air oven at 373 K after ageing for 24 hours at room temperature. The dried powder was then pulverised with a mortar and pestle before being calcined in a muffle furnace at 523 K for two hours in a silica crucible. In DC glow discharge air plasma, the

synthesised samples are exposed to different exposure times and schematic representation is shown in figure 1 a.

#### 2.4. Agar Well Diffusion Assay

The pure HAP and Ti doped HAP samples were dissolved in DMSO and evaluated for antibacterial activity using the good diffusion method before and after plasma treatment. The liquid Mueller Hinton agar media and Petri plates were autoclaved for 30 minutes at 15 pounds of pressure at 121° C. Under aseptic circumstances, around 20ml of agar media was dispensed onto each Petri plate in the laminar airflow chamber, resulting in a consistent depth of 4mm. After the media had set, *Bacillus cereus* (MTCC 430), *Staphylococcus aureus* (MTCC 3160), *E. coli* (MTCC 1698), and *Pseudomonas aeruginosa* (MTCC424) cultures were swabbed on the surface of the agar plates. A cork borer was used to create wells, and 50 µl and 100 µl of each sample were placed in separate wells, with DMSO serving as a negative control and Vancomycin (30mcg/disc) serving as a positive control [26]. The sample-loaded plates were incubated at 37°C for 24 hours to observe the zone of inhibition.

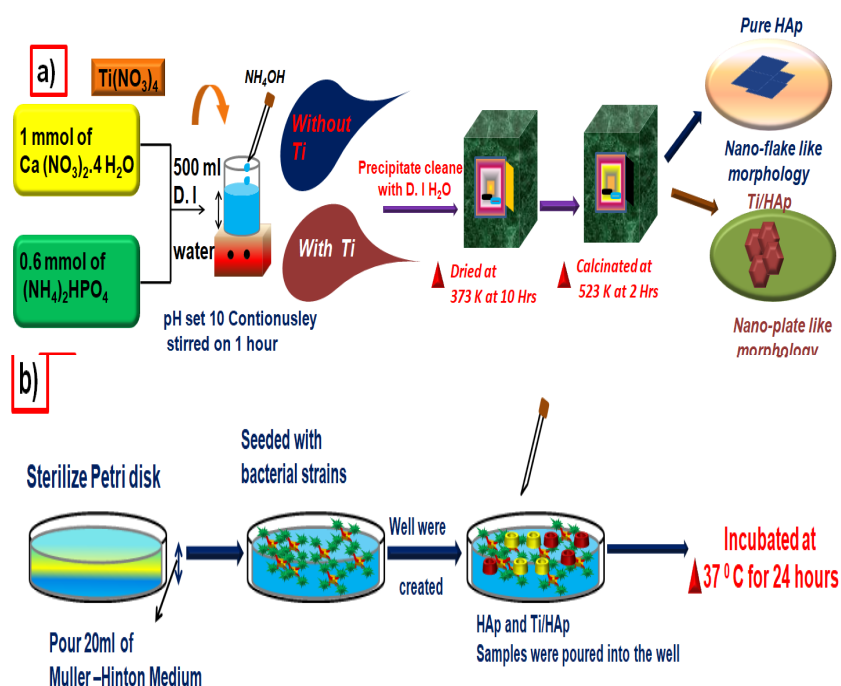


Fig. 1. (a) shows the schematic representation of pure HAP and Ti doped HAP synthesis procedure; (b) depicts the schematic representation of agar well diffusion method.

### 3. Result and discussions

#### 3.1. X-ray diffraction pattern (XRD)

Fig 2 (a) shows the XRD result of pure HAP and various time plasma treated (5, 10, 15 min) Ti-doped HAP samples at 400 volts DC voltage. The diffraction peaks of all the samples show reflections with strong intensity peaks at (211), (300), (002), and (004) miller planes, revealing the hexagonal structure, according to JCPDS card no. # 09-0432 for hydroxyapatite [27, 28]. Before and after plasma treatment, the XRD pattern of  $\text{TiO}_2$  doped HAP showed almost similar peaks with no obvious phase shift. Debye Scherrer's formula was used to compute the average crystallite size of pure HAP and Ti-doped HAP nanopowders [29]. According to the XRD pattern, treating the sample with air plasma for various exposure times resulted in only slight variations in intensity values. Variations in air plasma treatment time do not affect the results [30, 31]. Table 1 shows the different kinetic parameters of untreated pure HAP and treated Ti-doped HAP samples.

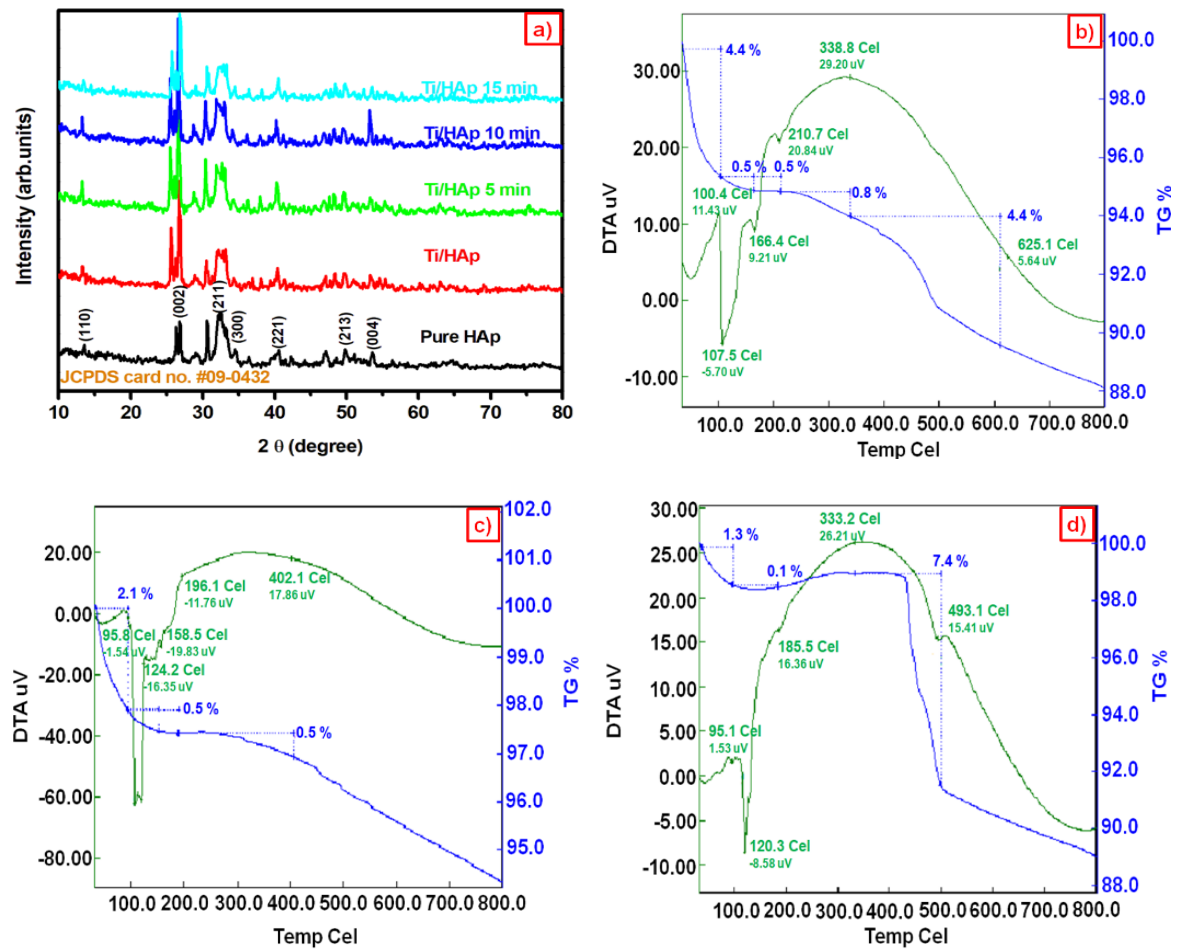


Fig. 2. (a) shows XRD images of pure HAp and Ti doped HAp samples with different plasma exposed like 5 min, 10 min and 15 min; (b) shows the TG-DTA analysis of pure HAp samples; (c) shows TG-DTA analysis of untreated Ti/HAp sample; (d) shows TG-DTA analysis of 15 min plasma treated Ti/HAp sample.

Table 1. Shows the different kinetic parameters of untreated pure HAp and treated Ti-doped HAp samples.

S. No.	Samples	Average Crystallite size D (nm)	Lattice Parameters (Å)		Unit cell Volume V (Å) <sup>3</sup>	Microstrain ( $\epsilon$ ) x 10 <sup>-3</sup> m	Dislocation density ( $\delta$ ) x 10 <sup>15</sup> / m <sup>2</sup>
			a = b	c			
1.	Pure HAp	35.66	9.5076	6.81	523.01	8.6154	26.313
2.	Untreated Ti/HAp	35.33	9.3733	6.9047	525.36	3.782	1.0946
3.	5 minutes Treated Ti/HAp	28.668	9.3562	6.9121	524.01	4.0425	1.3245
4.	10 minutes Treated Ti/HAp	33.58	9.3117	6.9504	521.9	3.3011	1.638
5.	15 minutes Treated Ti/HAp	39.45	9.2996	6.8247	511.14	2.8731	1.5591

### 3.2. Differential Thermal and Thermo Gravimetric (DT-TG) Analysis

In fig 2 shows the TG-DTA analysis of pure HAp, untreated Ti/HAp and 15 min plasma treated Ti/HAp samples. Fig 2 (b) shows the TG-DTA analysis of the pure HAp sample. The presence of OH groups causes a sharp weight loss of (4.4 %) at 100.4°C for untreated pure HAp, and it decomposes progressively above this temperature. For untreated pure HAp, a progressive decomposition was seen between 107.4°C and 625.1°C. Figures 2 (c) and 2 (d) show the plots of thermogravimetric analysis of untreated and 15 min plasma-treated Ti-doped HAp (b). At 95.8 ° C, the weight loss is (2.1%), and temperatures higher than this disintegrate gradually. For untreated Ti-doped HAp, a breakdown was reported between 108.6° C and 402.1° C. The weight loss (1.3 %) for plasma-treated Ti/ HAp occurs at 95.1 °C, and it decomposes above this temperature. For plasma-treated samples, the breakdown was recorded between 120.3° C and 493.1° C. The removal of moisture from the surface of HAp NPs causes the initial mass loss, which happens between 95.8 ° C and 124.2 ° C. Due to the evaporation of several volatile chemicals present in the sample; continued heating resulted in steady mass loss. Ti/HAp is thermally stable up to 800 ° C, according to the TG study.

### 3.3. Scanning electron microscopy (SEM) and Energy Dispersive X-Ray (EDAX) analysis

Surface morphology and elemental identification of pure HAp, untreated Ti/HAp, and plasma-treated Ti/HAp samples are shown in fig 3. Fig 3 (a) shows the nano-flake like morphology of a pure HAp sample with 0.5 µm. In fig 3 (b-e) shows SEM images of Ti-doped HAp samples with different times plasma treated.

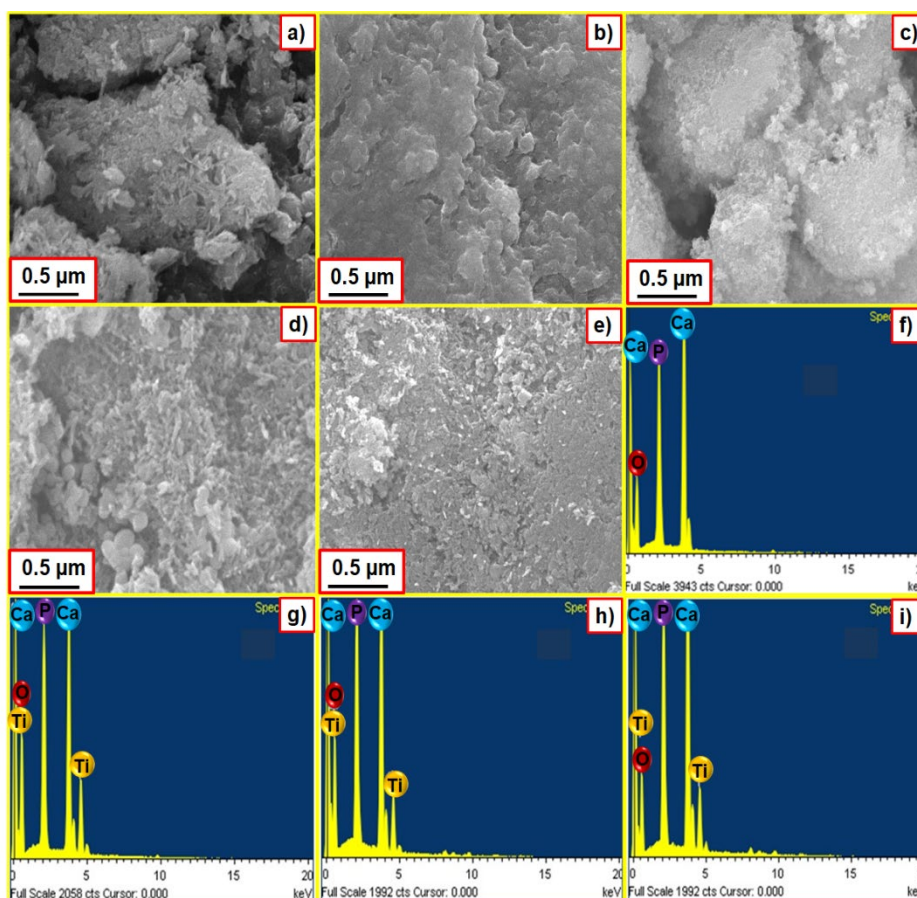


Fig. 3. Shows the SEM and EDAX images of pure HAp and Ti doped HAp samples with different plasma exposed like 5 min, 10 min and 15 min with different magnifications; (a) shows the SEM image of pure HAp sample; (b-e) shows the SEM image of untreated Ti/HAp and 5, 10, 15 min plasma treated Ti/HAp sample; (f-i) shows the EDAX results of pure HAp, untreated Ti/HAp and different plasma exposed Ti/HAp samples.

The particles were found to have a virtually platelet shape and agglomerated due to the Vander Waals force of attraction [32]. Because of the surface etching of air plasma, the morphology has improved. Figure 3 (f - i) shows the EDAX patterns of untreated HAp and plasma-treated Ti/HAp. The presence of Ti, O, P, and Ca in the elemental composition validates the components present in Ti/HAp [33]. There are no other impurity peaks or components evident save for a small change in oxygen content.

### 3.4. Fourier transform infrared spectral analysis (FTIR)

The pure HAp, Ti/HAp and various time plasma treated Ti/HAp samples FTIR results were shown in fig 4 (a). The presence of the hydroxyl group was given to the band at  $3429.94\text{ cm}^{-1}$ . The existence of  $\text{PO}_4^{3-(4)}$  is shown by the peak at  $566.59\text{ cm}^{-1}$ . Phosphate stretching vibration was confirmed by the band at  $1031.92\text{ cm}^{-1}$ [34]. The HAp crystallite surface has a wide range of absorption bands at  $3569\text{ cm}^{-1}$  and  $3429.94\text{ cm}^{-1}$  (OH) stretching and vibration modes [35]. Along with HAp, broadband around  $3400\text{--}3600\text{ cm}^{-1}$  can be linked to water or hydrated layer. The presence of  $(\text{CO}_3^{2-})$  at  $\text{PO}_4^{3-}$  sites are most likely the result of sample processing in air plasma. Variation in the plasma exposure period resulted in a rise in  $\text{CO}_3^{2-}$  vibration intensity over time. At  $3569.79\text{ cm}^{-1}$  (stretched) and  $632.17\text{ cm}^{-1}$ , the OH vibrations are well-defined (bending). The functional group remains the same in the band measured before and after plasma treatment, but the peak narrows as the plasma exposure period increases [36-38].

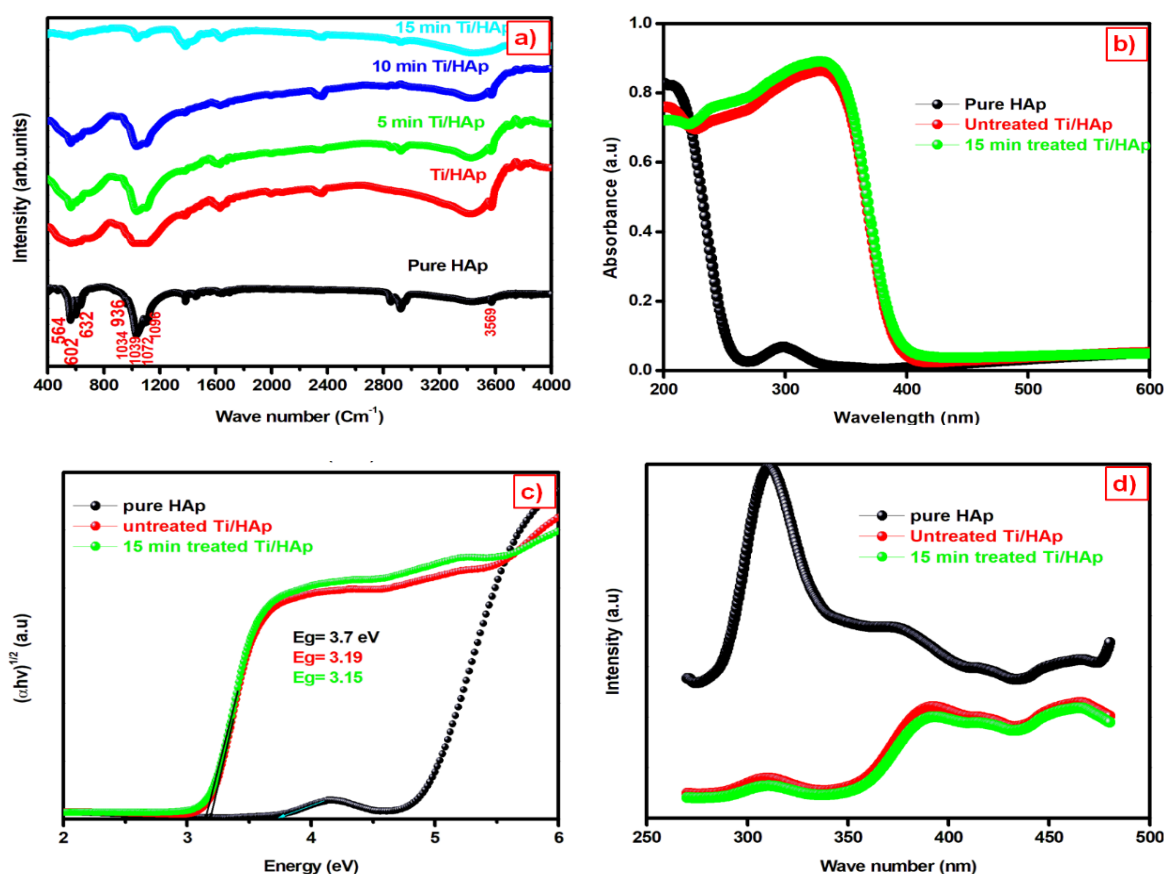


Fig. 4. (a) shows the FTIR images of pure HAp and Ti doped HAp samples with different plasma exposed like 5 min, 10 min and 15 min. (b) shows the UV result of pure HAp, untreated Ti/HAp and 15 min plasma treated Ti/HAp; (c) shows the K-M model band gap determination of pure HAp, untreated Ti/HAp and 15 min plasma treated Ti/HAp; (d) shows room temperature of photoluminescence spectra of pure HAp, untreated Ti/HAp and 15 min plasma treated Ti/HAp.

### 3.5. UV-vis spectral analysis

The optical absorption properties of pure untreated HAp, Ti/HAp, and 15 minutes plasma treated Ti/HAp materials were investigated using UV – vis absorption spectral analysis, as shown in Fig 4 (b). The spectra are in ultraviolet-visible light (UV-vis), and the band edge absorption in pure and Ti/HAp materials is observed at 295 nm and 330 nm of wavelength, respectively. The spectrum gives information on the electronic transitions that occur in the substance. Because spectra are normally given in wavelength units, the De Broglie relationship [39] is used to convert band gap energy (eV) units.

$$\Delta E = hc/\lambda \quad (\text{eV}) \quad (1)$$

where, h- Planck's constant, c- velocity of light, and  $\lambda$  -maximum wavelength. In fig 4 (c) shows the tauc plot of pure HAp, Ti/HAp and 15 minutes plasma treated Ti/HAp samples. Table 2 shows the computed bandgap in the absorption spectrum that corresponds to the point where absorption occurs, as well as the minimal amount of energy required for a photon to excite an electron across the bandgap from a lower to a higher energy level. As a result, the magnitude of the peak in the absorption spectra is slightly reduced by plasma treatment, but the bandgap energy does not change significantly.

Table 2. Shows UV Absorption Spectra and Peak Intensity for pure HAp , untreated Ti/HAp and 15 minutes plasma treated Ti/HAp.

Absorption peak position (nm)			Intensity (a.u)			Band gap energy (eV)		
Pure HAp	Untreated Ti/HAp	15 min Plasma treated Ti/ HAp	Pure HAp	Untreated Ti/HAp	15 min Plasma treated Ti/ HAp	Pure HAp	Untreated Ti/HAp	15 min Plasma treated Ti/ HAp
295	328	328	0.0682	0.891	0.864	3.7	3.19	3.15

### 3.6. Photoluminescence spectroscopy (PL)

Figure 4 (d) displays the photoluminescence spectra of untreated pure HAp, Ti/HAp, and 15-minute plasma-treated Ti/HAp samples. The luminescence peak of untreated pure HAp, Ti/HAp, and 15 minutes plasma treated Ti/HAp samples showed a broad visible emission band at 311, 310.5, and 310 nm, respectively. The spin-orbit coupling of six electrons in the f-subshell is demonstrated by these luminescence changes, which are attributable to the mixing of odd terms due to the crystal field. The presence of Ti in the HAp host is indicated by the non-degenerate transition. The recombination of excited electron-hole pairs causes PL emission, and low emission intensity suggests a low recombination rate [40].

### 3.7. Mechanical properties of Vickers hardness studies

Figure 5 shows the mechanical property using Vicker's hardness test with Hv as the Vicker's hardness number in  $\text{kg/mm}^2$ . Hv and MPa values for HAp before and after 15 minutes of plasma treatment are tabulated in table 4.5. In table 3 shows the HV and MPa values of untreated pure HAp, Ti/HAp and 15 minutes plasma treated Ti/HAp samples. As the applied stress rises from 25 to 100 grammes, grain boundary strengthening causes the microhardness rating to rise. Crack initiation occurs when the applied force exceeds 100 gm, which could be related to internal tension [41]. The plasma exposed Ti/HAp has high mechanical strength than untreated pure HAp and Ti/HAp samples.

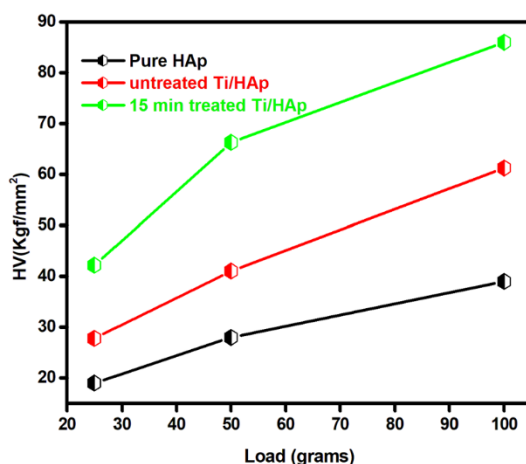


Fig. 5. Shows Vickers hardness analysis of pure HAp, untreated Ti/HAp and 15 min plasma treated Ti/HAp samples.

Table 3. Shows Vicker's Hardness results of pure HAp pure HAp , untreated Ti/HAp and 15 minutes plasma treated Ti/HAp.

Pure HAp and Ti/HAp						
Load (Grams)	H <sub>v</sub> (kgf/mm <sup>2</sup> )			MPa		
	Pure HAp	Untreated Ti/HAp	15 min treated Ti/HAp	Pure HAp	Untreated Ti/HAp	15 min treated Ti/HAp
25	19.65	27.8	42.2	192.7	272.6	413.9
50	29.15	41.05	66.3	285.9	402.6	650.2
100	40.35	61.25	86	395.7	600.7	843.4

### 3.8. Antibacterial analysis

#### 3.8.1. Bacterial Strains

Gram-positive bacteria including *Bacillus cereus* (MTCC 430), *Staphylococcus aureus* (MTCC 3160), and Gram-negative bacteria like *E.coli* (MTCC 1698) and *Pseudomonas aeruginosa* (MTCC424) were obtained from IMTECH in Chandigarh, India. For additional research, these strains were kept on nutrient agar.

#### 3.8.2. Antibacterial activity of prepared samples

The antibacterial result of pure HAp against *Bacillus cereus*, *Staphylococcus aureus*, *Escherichia coli*, and *Pseudomonas aeruginosa* bacteria is shown in Fig 6. The antibacterial activity of untreated Ti/HAp and plasma-treated Ti/HAp samples is shown in Fig 7. Fig 7 (a-d) shows the antibacterial activity of untreated Ti/HAp against *Bacillus cereus*, *Staphylococcus aureus*, *Escherichia coli*, and *Pseudomonas aeruginosa* bacteria. Antibacterial activity of 5, 10, and 15 minutes Ti/HAp against *Bacillus cereus*, *Staphylococcus aureus*, *Escherichia coli*, and *Pseudomonas aeruginosa* bacteria is shown in fig 7 (e-p). The antibacterial inhibition of the pure HAp and titanium substituted HAp before and after plasma treatment studied by agar well diffusion technique against the bacteria are listed the Table (3&4). Bacterial reduces after 15 minutes Plasma therapy is a treatment that involves the administration of According to Ti/HAp samples, exposing the material to air plasma improved its antibacterial activity. All 15-minute plasma-treated Ti/HAp samples indicate viable cell reduction of all bacteria, according to the results of the quantitative antimicrobial tests. The interaction of titanium particles with the release of titanium ions penetrate in the cellular envelope of bacteria may account for the antibacterial effect of the Ti/HAp sample following plasma treatment. This results in structural alterations, mostly in the cytoplasmic membrane, and may result in cell death [42].

## 8.9. In Vitro Cytotoxicity Studies

### 8.9.1. Cell Lines

The National Centre for Cell Science (NCCS) in Pune provided the human MCF-7 breast cancer cells and 3T3 fibroblast cells, which were cultured in Eagles Minimum Essential Medium containing 10% foetal bovine serum (FBS). The cells were kept at 37 ° C, 5% CO<sub>2</sub>, 95% air, and 100% relative humidity. The culture media was changed twice a week and the cultures were passed once a week.

### 8.9.2. MTT Assay and Protocol

MTT Cell is an in vitro proliferation and viability assay for determining cell growth or metabolic processes that contribute to apoptosis or necrosis. The suspension of untreated pure HAp and 15 minutes plasma treated Ti/HAp were added separately at concentrations (6, 12, 25, 55, and 85 g/L respectively) including 60 g/  $\mu$ L, 120 g/  $\mu$ L, 250 g/  $\mu$ L, 550 g/  $\mu$ L, 850 g/  $\mu$ L for all the samples with the reference medication. The cells are treated according to the experimental design, and the incubation periods for each cell type and system are tuned. MTT (3-[4, 5-dimethylthiazol-2-yl]-2, 5-diphenyltetrazolium bromide) is a tetrazolium chemical that is added to the wells and incubated with the cells [43]. MTT is converted to insoluble purple formazan dye crystals by metabolically active cells. The wells are then treated with detergent, which dissolves the crystals and allows the absorbance to be measured with a spectrophotometer [44]. The samples are directly read in the wells. The best wavelength for absorbance is 570 nm, and the data is examined by plotting extract concentration versus absorbance, which allows quantification of cell proliferation variations. The pace at which tetrazolium is depleted is linked to the rate at which cells proliferate.

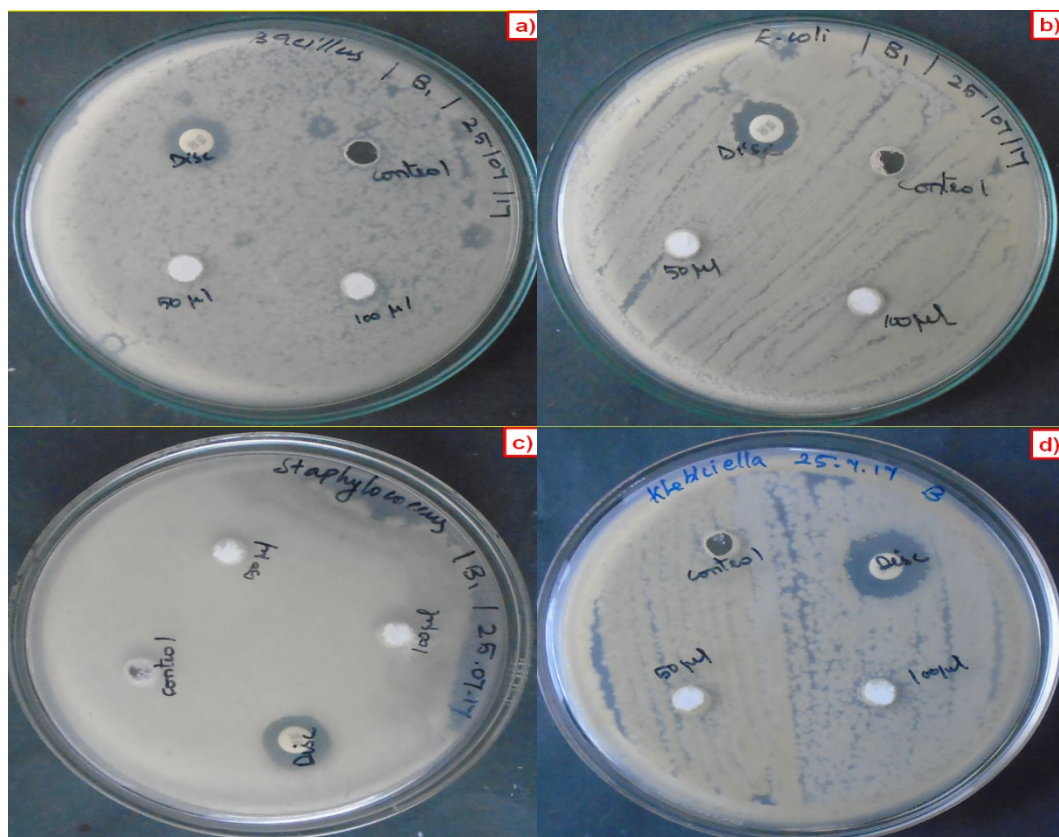


Fig. 6. Shows pure HAp samples antibacterial activity against gram positive and gram negative bacteria's.

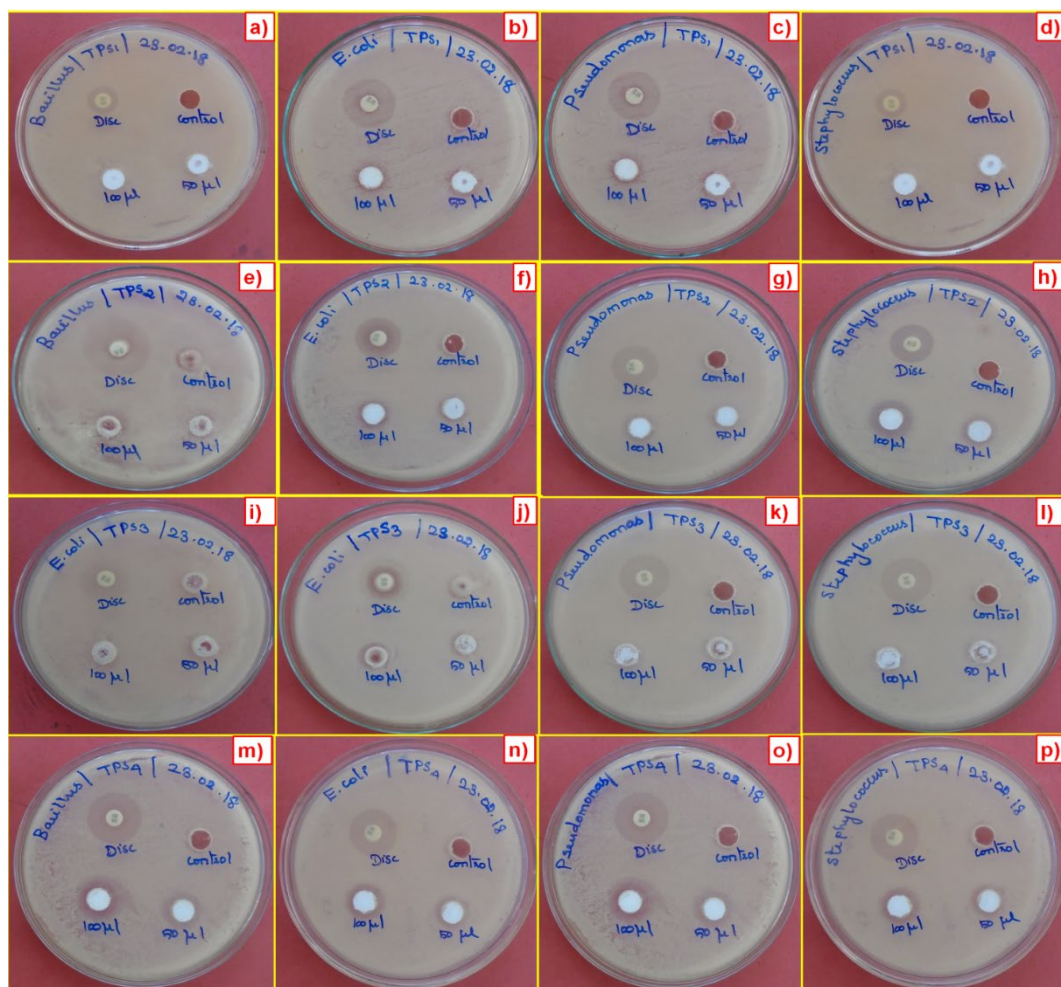


Fig. 7. Shows antibacterial activity of untreated Ti/HAp and various time plasma treated Ti/HAp samples; (a-d) shows the untreated Ti/HAp sample antibacterial activity against gram positive and gram negative bacteria's; (e-h) shows the 5 min plasma treated Ti/HAp sample antibacterial activity against gram positive and gram negative bacteria's; (i-l) shows the 10 min plasma treated Ti/HAp sample antibacterial activity against gram positive and gram negative bacteria's; (m-p) shows the 15 min plasma treated Ti/HAp sample antibacterial activity against gram positive and gram negative bacteria's.

Table 4. Shows Zone inhibition values of pure Hap, Ti/HAp and plasma treated Ti/HAp samples against gram positive bacteria.

S. No	Samples	Zone inhibition of gram positive bacteria in mm			
		Bacillus cereus		Staphylococcus aureus	
		50 µl	100 µl	50 µl	100 µl
	<b>Standard vancomycin</b>	14		21.5	
1.	Pure HAp	Nil	Nil	Nil	Nil
	<b>Standard vancomycin</b>	15		16	
2.	Ti/HAp	Nil	Nil	Nil	Nil
3.	5 min treated Ti/HAp	9	12	Nil	Nil
4.	10 min treated Ti/HAp	Nil	Nil	Nil	Nil
5.	15 min treated Ti/HAp	8	13	9	11

Table 5. Shows Zone inhibition values of pure HAp, Ti/HAp and plasma treated Ti/HAp samples against gram negative bacteria.

S. No	Samples	Zone inhibition of gram negative bacteria in mm			
		E.coli		Pseudomonas aeruginosa	
		50 $\mu$ l	100 $\mu$ l	50 $\mu$ l	100 $\mu$ l
<b>Standard vancomycin</b>		<b>15</b>		<b>12</b>	
1.	Pure HAp	Nil	Nil	Nil	Nil
<b>Standard vancomycin</b>		<b>15</b>		<b>15</b>	
2.	Ti/HAp	Nil	Nil	Nil	Nil
3.	5 min treated Ti/HAp	Nil	Nil	Nil	Nil
4.	10 min treated Ti/HAp	Nil	Nil	Nil	Nil
5.	15 min treated Ti/HAp	10	13	8	12

### 8.9.3. *In Vitro* Cytotoxic Effect for 3T3 Cell Line

The MTT test was used to measure the mean per cent cell viability of synthesised untreated Ti/HAp and 15 minutes plasma treated Ti/HAp samples against 3T3 Fibroblast cell lines at varying doses (6 g/ $\mu$ L - 85 g/ $\mu$ L). Figure 8 shows an image of the MTT assay as well as a bar graph for control on the 3T3 fibroblast cell line. Cell proliferation was investigated using a dose-dependent percentage of cell viability for the samples. Under a phase-contrast microscope, morphological changes in the 3T3 cell line were identified after exposure to the synthesised materials. The Trypan blue exclusion method was used to estimate the percentage of viable cells [45]. The bar graph of untreated Ti/HAp and 15 minutes plasma treated Ti/HAp samples are shown in Fig 9. The fibroblast cell line is nontoxic to the synthesised untreated Ti/HAp and 15 minutes plasma treated Ti/HAp, according to the percentage of cell viability and OD values calculated in the figure. These *in vitro* results showed that the synthesized Ti/HAp before and after plasma treatment were nontoxic for 3T3 fibroblast cells [46].

### 8.9.4. *In Vitro* Cytotoxic Effect for MCF - 7 Cell Line

The synthesized HAp and Ti/HAp before and after 15 Min. air plasma exposure was screened for their cytotoxicity against human MCF-7 Breast cancer cell lines at different concentrations (6  $\mu$ g/ $\mu$ L - 85  $\mu$ g/ $\mu$ L), to determine the mean per cent (%) cell viability by MTT assay. On cell proliferation, a dose-dependent percentage of cell viability of hydroxyapatite samples was investigated. All cytotoxic activity was measured over 24 hours. The antiproliferative actions of synthesised untreated Ti/HAp and 15 minutes plasma treated Ti/HAp on the growth of MCF-7 Breast cancer cell lines were discovered before and after plasma exposure. Figure (10 & 11) represents the image of MTT assay and bar graph for control on MCF-7 Breast cancer cells line. MCF-7 cell line morphological changes after exposure to untreated Ti/HAp and plasma-treated Ti/HAp for 15 minutes. The Trypan blue exclusion method was utilized to predict the percentage of cell viability on cytostatic effects. The untreated Ti/HAp and 15 minutes plasma treated Ti/HAp at 85  $\mu$ g/ $\mu$ L showed the better antiproliferative effect. The prepared samples show a superior effect on treated MCF-7 cells as compared to untreated cells, according to microscopic examinations. In terms of observation, the number of dead cells rose in lockstep with the sample treatment concentration increase. The cells became noticeably larger when the extract concentration was high. Membrane blebbing, apoptotic bodies and ballooning were visible in about 40 per cent to 50 per cent of the cells. Cells also showed extensive vacuolation in the cell cytoplasm, indicating autophagy like a mechanism of cell death [47]. The cells grew rounder, smaller, and showed evidence of separation from the well surface at the maximum concentration (85  $\mu$ g/L), indicating cell death.

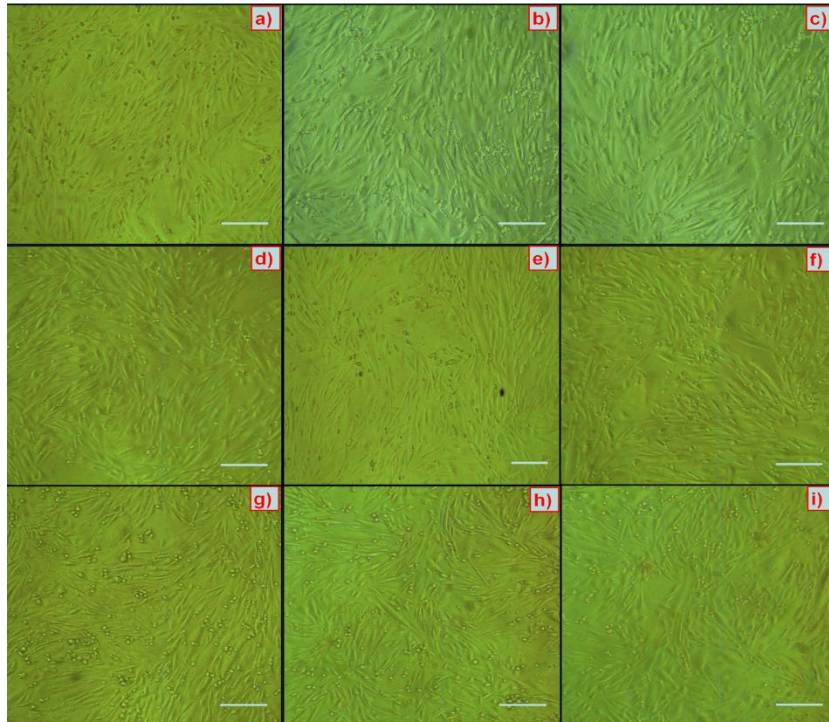


Fig. 8. Shows images of MTT assay on 3T3 Cell line; (a) Control on 3T3 Cell line; (b, c) Low dose and high dose of Pure HAp samples; (d, e) Low dose and high dose of untreated Ti/HAp sample; (f, g) Low dose and high dose of 5 min plasma treated Ti/HAp sample; (h, i) Low dose and high dose of 15 min plasma treated Ti/HAp sample.

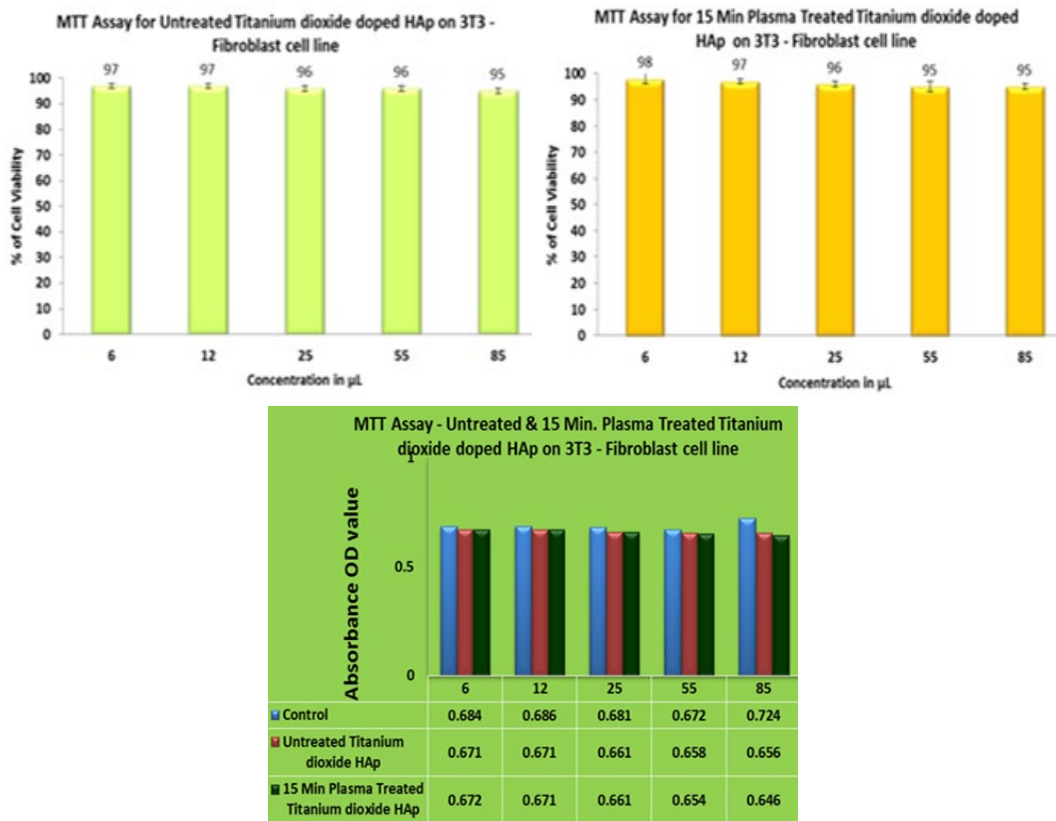
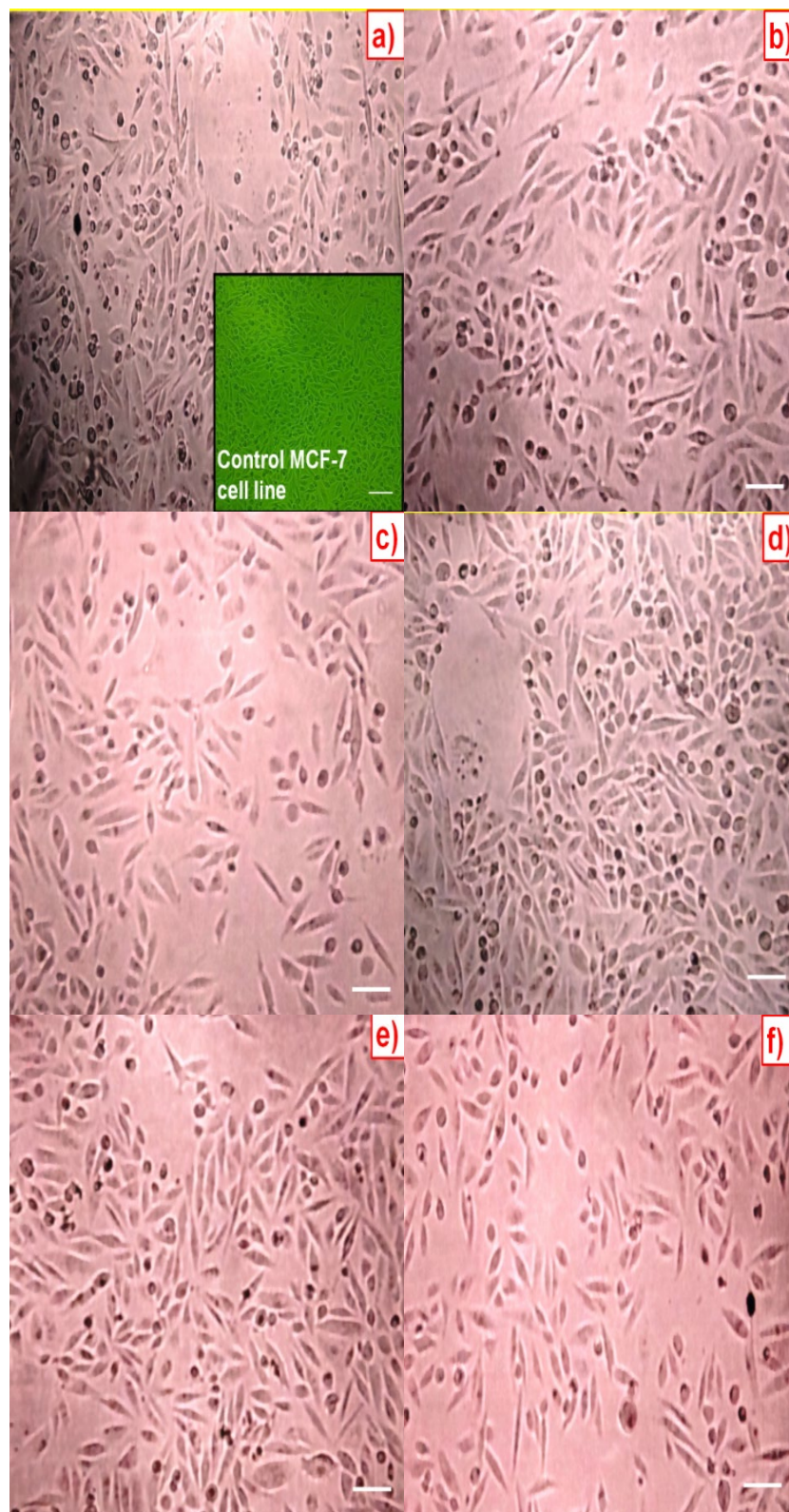


Fig. 9. Shows Bar graph for Titanium di oxide doped HAp on 3T3 - Fibroblast cell line.



*Fig. 10. Shows Images of MTT assay on MCF- 7 Cell line; (a-c) Low, medium and high dose of untreated Ti/HAp samples; (d-f) Low, medium and high dose of 15 min plasma treated Ti/HAp samples.*

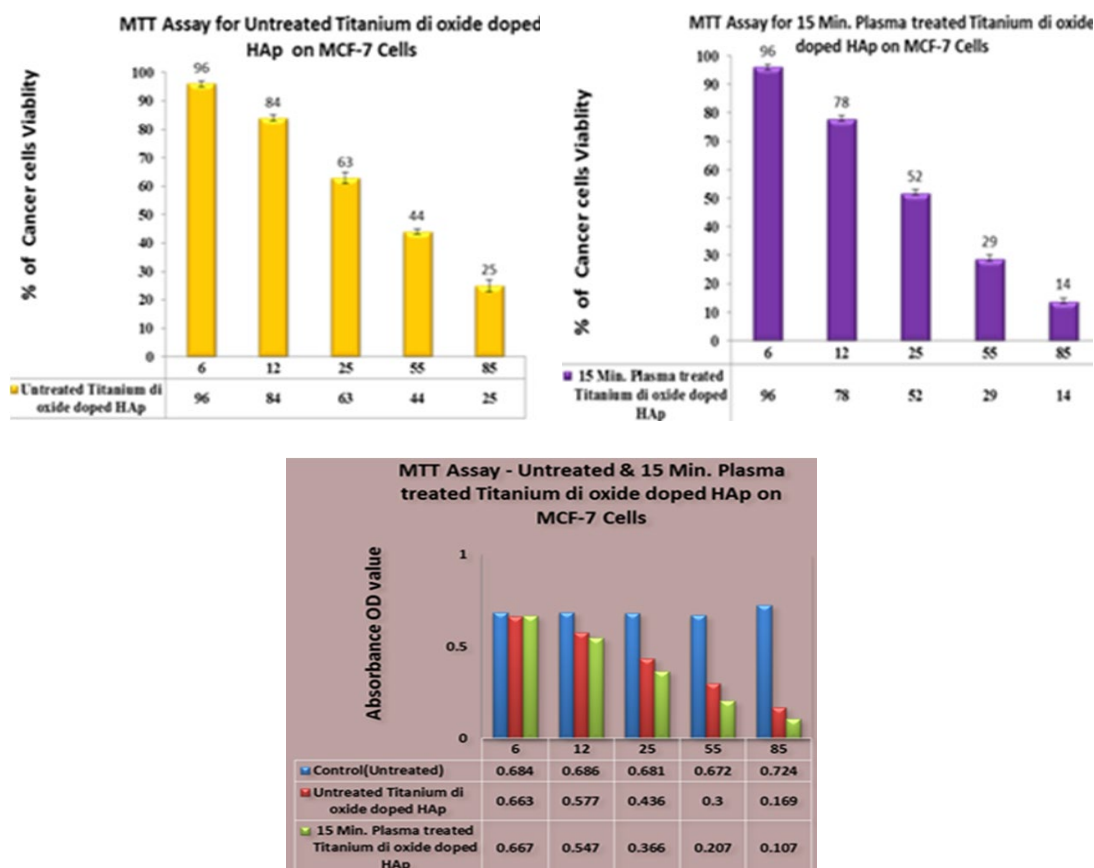


Fig. 11. Shows Bar graph for Titanium doped HAp on MCF-7 - Cancer cell line.

## 9. Conclusion

The Pure HAP and Ti/HAp nanoparticles were successfully generated in this study utilising a simple sol-gel enhanced with DC light discharge plasma approach HAp by varying the plasma exposure times. The XRD, SEM, EDAX, TG-DTA, FTIR, antibacterial activity and cytotoxicity of pure HAp and zinc doped HAp samples are characterised using various analytical techniques for bone graft substitute. Untreated pure HAp, Ti/HAp and 5, 10, 15 minutes plasma treated Ti/HAp samples have good antibacterial activity against two Gram-positive bacteria, *Bacillus cereus* and *Staphylococcus aureus*, as well as two Gram-negative bacteria, *E. coli* and *Pseudomonas aeruginosa*. The pure HAp the Ti/HAp possesses substantial cytotoxicity activity, as evidenced by the above experiment. This makes it a precise material for bone replacement in biomedical applications. Different concentrations of Ti/HAp were investigated for cytotoxicity against 3T3 Fibroblast cell lines and human MCF-7 Breast cancer cell lines, according to the findings. These *in vitro* results showed that the synthesized Ti/HAp before and after plasma treatment were nontoxic for 3T3 fibroblast cells. On MCF-7 breast cancer cell lines, both the untreated and plasma-treated samples had antiproliferative effects.

## References

- [1] H.J. Pérez-Cano, A. Robles Contreras, Basic aspects of the mechanisms of bacterial resistance, *Rev. Médica MD* 4 (2013) 186-191 <https://revistamedicamd.com/>.
- [2] G. Martelli, D. Giacomini, Antibacterial and antioxidant activities for natural and synthetic dual-active compounds, *Eur. J. Med. Chem.* 158 (2018) 91-105; <https://doi.org/10.1016/j.ejmech.2018.09.009>

- [3] WHO, Antibiotic-resistance, World Health Organization; Newsroom., 2018, <https://www.who.int/news-room/fact-sheets/detail/antibiotic-resistance>.
- [4] B. Thornes, P. Murray, D. Bouchier-Hayes, Development of resistant strains of *Staphylococcus epidermidis* on gentamicin-loaded bone cement in vivo, *J. Bone Joint Surg. Br.* 84 (2002) 758-760; <https://doi.org/10.1302/0301-620X.84B5.0840758>
- [5] D. Campoccia, L. Montanaro, P. Speziale, C.R. Arciola, Antibiotic-loaded bio-materials and the risks for the spread of antibiotic resistance their prophylactic and therapeutic clinical use, *Biomaterials* 31 (2010) 6363-6377; <https://doi.org/10.1016/j.biomaterials.2010.05.005>
- [6] A. Dion, M. Langman, G. Hall, M. Filiaggi, Vancomycin release behaviour from amorphous calcium polyphosphate matrices intended for osteomyelitis treatment, *Biomaterials* 26 (2005) 7276-7285; <https://doi.org/10.1016/j.biomaterials.2005.05.072>
- [7] M.Á. Serra-Valdés, Microbial resistance in the current context and the importance of knowledge and application in antimicrobial policy, *Rev. Habanera Ciencias Méd.* 5 (2017) 8-9 <http://www.revhabanera.sld.cu/index.php/rhab/article/view/2013>.
- [8] Ž. Radovanović, B. Jokić, D. Veljović, S. Dimitrijević, V. Kojić, R. Petrović, D. Janačković, Antimicrobial activity and biocompatibility of Ag<sup>+</sup> and Cu<sup>2+</sup> doped biphasic hydroxyapatite/ $\alpha$ -tricalcium phosphate obtained from hydrothermally synthesized Ag<sup>+</sup> and Cu<sup>2+</sup> doped hydroxyapatite, *Appl. Surf. Sci.* 307 (2014) 513-519; <https://doi.org/10.1016/j.apsusc.2014.04.066>
- [9] M.H. Corona Carpio, Y. Hernandez Espinosa, I. Mondelo Lopez, Y.E. Castro Sanchez, L. Diaz del Mazo, Main factors provoking dental implant failure, *Medisan* 19 (2015) 1325-1329.
- [10] T. Zhou, Y. Zhu, X. Li, X. Liu, K.W.K. Yeung, S. Wu, X. Wang, Z. Cui, X. Yang, P.K. Chu, Surface functionalization of biomaterials by radical polymerization, *Prog. Mater. Sci.* 83 (2016) 191-235; <https://doi.org/10.1016/j.pmatsci.2016.04.005>
- [11] N.C. Reger, A.K. Bhargava, I. Ratha, B. Kundu, V.K. Balla, Structural and phase analysis of multi-ion doped hydroxyapatite for biomedical applications. *Ceram Int.* 45, (2019) 252-63; <https://doi.org/10.1016/j.ceramint.2018.09.160>
- [12] T.M. Andrade, D.C. Mello, C.M. Elias, J.M. Abdala, E. Silva, L.M. Vasconcelos, In vitro and in vivo evaluation of rotaryjet-spun poly ( $\epsilon$ -caprolactone) with high loading of nanohydroxyapatite. *J Mater Sci: Mater Med.* 30 (2019) 19; <https://doi.org/10.1007/s10856-019-6222-1>
- [13] S. Aarthy, D. Thenmuhil, G. Dharunya, P. Manohar, Exploring the effect of sintering temperature on naturally derived hydroxyapatite for bio-medical applications. *J Mater Sci: Mater Med.* 30 (2019) 21; <https://doi.org/10.1007/s10856-019-6219-9>
- [14] S.L. Bee, Z.A.A. Hamid, Hydroxyapatite derived from food industry bio-wastes: syntheses, properties and its potential multifunctional applications. *Ceram Int.* 46 (2020) 17149-75; <https://doi.org/10.1016/j.ceramint.2020.04.103>
- [15] G. Fernandez de Grado, L. Keller, Y. Idoux-Gillet, Q. Wagner, A.M. Musset, N. Benkirane-Jessel, Bone substitutes: a review of their characteristics, clinical use, and perspectives for large bone defects management. *J Tissue Eng.* 9 (2018) 1-18; <https://doi.org/10.1177/2041731418776819>
- [16] M.C. Bottino, D. Pankajakshan, J.E. Nör, Advanced scaffolds for dental pulp and periodontal regeneration. *Dent Clin N Am.* 61 (2017) 689-711; <https://doi.org/10.1016/j.cden.2017.06.009>
- [17] Y. Su, I. Cockerill, Y. Zheng, L. Tang, Y.X. Qin, D. Zhu, Biofunctionalization of metallic implants by calcium phosphate coatings. *Bioact Mater.* 4 (2019) 196-206; <https://doi.org/10.1016/j.bioactmat.2019.05.001>
- [18] J. Adhikary, B. Das, S. Chatterjee, S.K. Dash, S. Chattopadhyay, S. Roy, J.-W. Chen, T. Chattopadhyay, Ag/CuO nanoparticles prepared from a novel trinuclear compound [Cu(Imdz)<sub>4</sub>(Ag(CN)<sub>2</sub>)<sub>2</sub>](Imdz=imidazole) by a pyrolysis display excellent antimicrobial activity, *J. Mol. Struct.* 1113 (2016) 9-17; <https://doi.org/10.1016/j.molstruc.2016.02.029>
- [19] H. Shah, B.A.M. Manikandan, V. Ganesan, Enhanced bioactivity of Ag/ZnO nanorods-a comparative antibacterial study (Sbds), *J. Nanomed. Nanotechnol.* 2013 (2013).
- [20] H. Zhang, G. Chen, Potent antibacterial activities of Ag/TiO<sub>2</sub> nanocomposite powders synthesized by a one-pot sol-gel method, *Environ. Sci. Technol.* 43 (2009) 2905-2910;

<https://doi.org/10.1021/es803450f>

- [21] S.A. Amin, M. Pazouki, A. Hosseinnia, Synthesis of TiO<sub>2</sub>-Ag nanocomposite with sol-gel method and investigation of its antibacterial activity against E. coli, Powder Technol. 196 (2009) 241-245; <https://doi.org/10.1016/j.powtec.2009.07.021>
- [22] G. Fu, P.S. Vary, C.-T. Lin, Anatase TiO<sub>2</sub> nanocomposites for antimicrobial 788 coatings, J. Phys. Chem. B 109 (2005) 8889-8898; <https://doi.org/10.1021/jp0502196>
- [23] Y. Zhang, L. Zhang, B. Li, Y. Han, Enhancement in sustained release of antimicrobial peptide from dual-diameter-structured TiO<sub>2</sub> nanotubes for long-lasting antibacterial activity and cytocompatibility. ACS applied materials & interfaces, 9(11), (2017) 9449-9461; <https://doi.org/10.1021/acsami.7b00322>
- [24] J. Han, J. Qi, J. Du, G. Zhang, Fabrication of chitosan hydrogel incorporated with Ti-doped hydroxyapatite for efficient healing and care of joint wound. Materials Letters, 278 (2020) 128415; <https://doi.org/10.1016/j.matlet.2020.128415>
- [25] M. Tsukada, M. Wakamura, N. Yoshida, T. Watanabe, Band gap and photocatalytic properties of Ti-substituted hydroxyapatite: Comparison with anatase-TiO<sub>2</sub>. Journal of Molecular Catalysis A: Chemical, 338(1-2) (2011) 18-23; <https://doi.org/10.1016/j.molcata.2011.01.017>
- [26] K.H. Prasad, V.R. Julakanti, G. Rangaraju, M. Sumithra, N. Sundaraganesan, July. Structural and Impedance Studies of Nanocrystalline LiCoO<sub>2</sub> Particle. In 2020 International Conference on System, Computation, Automation and Networking (ICSCAN) (1-4) (2020) IEEE; <https://doi.org/10.1109/ICSCAN49426.2020.9262338>
- [27] P. Sharma, A. Trivedi, H. Begam, Synthesis and characterization of pure and titania doped hydroxyapatite. Materials Today: Proceedings, 16 (2019) 302-307; <https://doi.org/10.1016/j.matpr.2019.05.094>
- [28] D. Shaw, A. West, J. Bredin, E. Wagenaars, S. Plas. Sci. Technol., 25, (1-6) (2016); <https://doi.org/10.1088/0963-0252/25/6/065018>
- [29] R. BoopathiRaja, M. Parthibavarman, Reagent induced formation of NiCo<sub>2</sub>O<sub>4</sub> with different morphologies with large surface area for high performance asymmetric supercapacitors. Chemical Physics Letters, 755 (2020) 137809; <https://doi.org/10.1016/j.cplett.2020.137809>
- [30] N. Karthikeyan, K.A. Vijayalakshmi, K. Vignesh, Functionalisation of viscose fabric with chitosan particles using non-thermal oxygen plasma. Materials Technology, 31(6), (2016) 358-363; <https://doi.org/10.1179/1753555715Y.0000000067>
- [31] A. Slepko, A.A. Demkov, W.Y. Loh, P. Majhi, G. Bersuker, Work function engineering in silicides: Chlorine doping in NiSi. Journal of Applied Physics, 109(8), (2011) 083703; <https://doi.org/10.1063/1.3573481>
- [32] Q. Zhang, L. Jiang, J. Wang, Y. Zhu, Y. Pu, W. Dai, Photocatalytic degradation of tetracycline antibiotics using three-dimensional network structure perylene diimide supramolecular organic photocatalyst under visible-light irradiation. Applied Catalysis B: Environmental, 277, (2020) 119122; <https://doi.org/10.1016/j.apcatb.2020.119122>
- [33] R. Mariappan, M. Ragavendar, V. Ponnuswamy, Growth and characterization of chemical bath deposited Cd<sub>1-x</sub>Zn<sub>x</sub>S thin films. Journal of alloys and compounds, 509(27), (2011) 7337-7343; <https://doi.org/10.1016/j.jallcom.2011.04.088>
- [34] Y. Yin, E. Liu, H. Li, J. Wan, J. Fan, X. Hu, J. Li, C. Tang, C. Pu, Fabrication of plasmonic Au/TiO<sub>2</sub> nanotube arrays with enhanced photoelectrocatalytic activities. Ceramics International, 42(8), (2016) 9387-9395; <https://doi.org/10.1016/j.ceramint.2016.02.157>
- [35] J. Kolmas, E. Groszyk, D. Kwiatkowska-Rohycka, BioMed Res. Int., 10, (2014), 1-15; <https://doi.org/10.1155/2014/178123>
- [36] R. Dorai, M.J. Kushner, A model for plasma modification of polypropylene using atmospheric pressure discharges. J. Phys. D J phys D Apply phys, 36(6), 2003) 666; <https://doi.org/10.1088/0022-3727/36/6/309>
- [37] Yang, J., Cui, F.Z., Lee, I.S. and Wang, X., Plasma surface modification of magnesium alloy for biomedical application. Surf. Coat, 205, (2010) 182-187; <https://doi.org/10.1016/j.surfcoat.2010.07.045>

- [38] S. Vijayakumar, B. Malaikozhundan, S. Shanthi, B. Vaseeharan, N. Thajuddin, Control of biofilm forming clinically important bacteria by green synthesized ZnO nanoparticles and its ecotoxicity on *Ceriodaphnia cornuta*. *Microb. Pathog*, 107, (2017) 88-97; <https://doi.org/10.1016/j.micpath.2017.03.019>
- [39] HairongYin, YanxiaoLi, JianguangBai, MingxinMa and JingLiu, *J. Materiom.*, 3, (2017), 144-149.
- [40] P. Sri Devi, K.A.Vijayalakshmi, *IAETSD J. Adv. Res. App. Sci.*, 5(1), (2018), 440 - 444.
- [41] V. Kalaiselvi, R. Mathammal, S. Vijayakumar, B. Vaseeharan, Microwave assisted green synthesis of Hydroxyapatite nanorods using *Moringa oleifera* flower extract and its antimicrobial applications. *int. j. vet. sci.*, 6(2), (2018) 286-295; <https://doi.org/10.1016/j.ijvsm.2018.08.003>
- [42] Nazari, A.G., Tahari, A., Moztaizadeh, F., Mozafari, M. and Bahrololoom, M.E., Ion exchange behaviour of silver-doped apatite micro-and nanoparticles as antibacterial biomaterial. *Micro Nano Lett.*, 6(8) (2011) 713-717; <https://doi.org/10.1049/mnl.2011.0381>
- [43] Qing, F., Wang, Z., Hong, Y., Liu, M., Guo, B., Luo, H. and Zhang, X., Selective effects of hydroxyapatite nanoparticles on osteosarcoma cells and osteoblasts. *J Mater Sci Mater Med*, 23(9) (2012) 2245-2251; <https://doi.org/10.1007/s10856-012-4703-6>
- [44] H. Wang, L. He, P. Zhang, J. Zhang, Z. Chen, X. Ren, X. Mei, Folate-modified hydroxyapatite nanorods induce apoptosis in MCF-7 cells through a mitochondrial-dependent pathway. *New J Chem*, 43(37) (2019)14728-14738; <https://doi.org/10.1039/C9NJ03653A>
- [45] W. Tang, Y. Yuan, C. Liu, Y. Wu, X. Lu, J. Qian, Differential cytotoxicity and particle action of hydroxyapatite nanoparticles in human cancer cells. *Nanomedicine*, 9(3), (2014) 397-412; <https://doi.org/10.2217/nnm.12.217>
- [46] X. Zhao, B.C. Heng, S. Xiong, J. Guo, T.T.Y. Tan, F.Y.C. Boey, K.W. Ng, J.S.C. Loo, In vitro assessment of cellular responses to rod-shaped hydroxyapatite nanoparticles of varying lengths and surface areas. *Nanotoxicology*, 5(2), (2011) 182-194; <https://doi.org/10.3109/17435390.2010.503943>
- [47] M. Nugoli, P. Chuchana, J. Vendrell, B. Orsetti, L. Ursule, C. Nguyen, D. Birnbaum, E.J. Douzery, P. Cohen, C. Theillet, Genetic variability in MCF-7 sublines: evidence of rapid genomic and RNA expression profile modifications. *BMC cancer*, 3(1), (2003) 1-12; <https://doi.org/10.1186/1471-2407-3-13>